Supplementary technical details

In this supplement, we provide the reader with a detailed description of how we closed the axial stress exerted by the tapered bottleneck and thus evaluated the equation of motion (16). If not indicated otherwise, cross references refer to the main document.

Supplement A. Constitutive law and sliding friction: model and experimental validation

According to the slenderness and the constitutive behaviour of the stopper anticipated in items (iii) and (iv) of § 2.1 and following Saadallah (2020) (see also Fernandes et al., 2014), we express the typical nonlinear dependence of $\tilde{\sigma}$ on the relative compression ε with sufficient accuracy as

$$\tilde{\sigma}_n(\varepsilon) = \tilde{A}\varepsilon^3 - \tilde{B}\varepsilon^2 + \tilde{C}\varepsilon\,, \qquad \varepsilon(z,t) = 1 - R(z,t)/r_C\big(z - Z(t)\big)\,, \tag{S 1}$$

The positive model coefficients $\tilde{A}$, $\tilde{B}$, $\tilde{C}$ must be determined empirically via a best fit. These together with a reliable estimate of a constant friction coefficient μ referring to the pairing cork/glass form the input parameters determining the mechanical behaviour of the cork.

Both $\tilde{\sigma}_n(\varepsilon)$ and the friction coefficient μ were sensed with due rigour by in-house testings. To this end, we employed a reciprocating standard tribometer to apply $\tilde{\sigma}_n$ quasi-statically and $\tilde{\sigma}_n$ in an oscillatory fashion on appropriate cork samples. To ensure a constant normal compressive stress acting normal to the contact surface, the setup typically requires a relatively small, cuboid or cylindrical sample to accomplish the first task. Therefore, a cuboid with dimensions $\tilde{D}_1 \times \tilde{D}_2 \times \tilde{D}_3 = 14.0 \times 12.5 \times 17.5\,\mathrm{mm}^3$ was cut out of the mid of a stopper. Given the constitutive behaviour outlined in item (iv) in § 2.1, here and below the indices refer to main axes of stress and strain. A normal compressive force $\tilde{F}_3$ was applied by a lever with a length ratio of one-to-five and a corresponding amount of weight hanged onto its other end. This yielded an indentation $\tilde{\delta}_3$ (> 0) measured via a laser beam and indeed no perceptible transverse expansion. A controlled stepwise increase of $\tilde{F}_3$ allowed for measuring the stress $\tilde{\sigma}_3 = \tilde{F}_3/(\tilde{D}_1\tilde{D}_2)$ as a function of the relative compression $\varepsilon_3 = \tilde{\delta}_3/\tilde{D}_3$. The observed uniaxial states of stress and strain confirm the stipulated constitutive properties of cork. With these in mind, a permutation of the axes is confidently supposed to leave the results essentially unchanged, and the measured quantities $\tilde{\sigma}_3$ and ε_3 can be identified with respectively $\tilde{\sigma}_n$ and ε for the axisymmetric case in (S 1). Hence, a least-square fit entailed $\tilde{A} = 30.608\,\mathrm{MPa}$, $\tilde{B} = 11.982\,\mathrm{MPa}$, $\tilde{C} = 4.200\,\mathrm{MPa}$ (rounded). The so recorded relationship $\tilde{\sigma}_n(\varepsilon)$ is depicted in figure S 1a.

The marked temporal increase $\tilde{\delta}_3$ at a constant load $\tilde{F}_3$ and correspondingly delayed approach of its terminal value, indicating the anticipated static dependence of $\tilde{\sigma}_3$ on ε_3, deserves mentioning. This creeping behaviour points to the inherent, but neglected, viscoelastic properties of cork. Even after approximately two minutes since the load had been applied, the stopper had not reached its final state yet. Likewise, a noticeable relaxation was observed when the load was released.

The dynamic measurements of μ were carried out with a real stopper sliding over a glass surface in a straightforward fashion. They confirm the suggestion by Fatima Vaz & Fortes (1998) that μ decreases slightly with increasing sliding speed. An analogous but more pronounced trend was revealed for increasing loads, $\tilde{F}_n$, applied normal onto the stopper and the glass plate underneath. Since the setup required the associated normal stress being definitely lower than $\tilde{\sigma}_n$ during the sliding of the stopper through the bottleneck, the found data shown in figure S 1b were extrapolated to suggest a nearly constant value of μ close to 0.2. This is the figure we used initially in our simulations. We emphasise that published measurements of μ are scarce, and the work by Fatima Vaz & Fortes (1998) represents an appreciated exception. Their experiments suggest μ being a factor 2 to 3 times higher, but the cork as well as the testing procedure they adopted differ from ours. Also, these authors mention the difficulty of obtaining reliable results in a systematic manner given the strong scatter of the data.

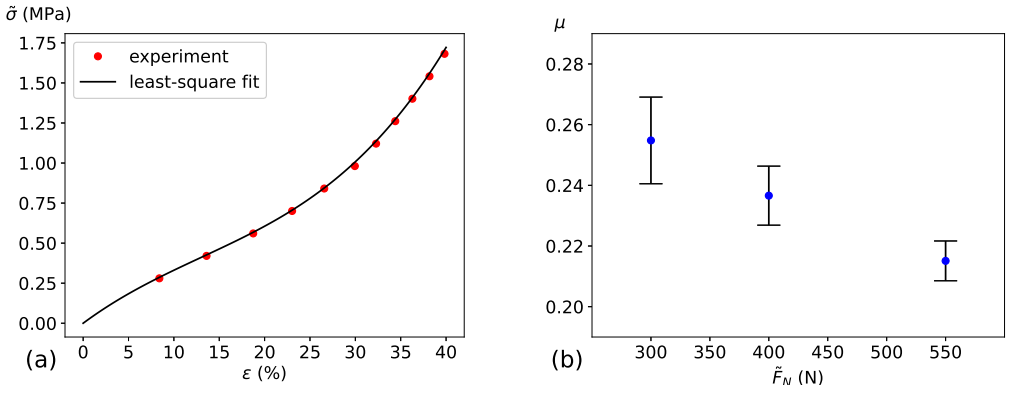

Figure S 1. *(a) Stress $\tilde{\sigma}_n$ exerted perpendicularly on stopper vs. its relative compression ε, (S 1); (b) friction coefficient μ by in-house experiments: mean values (blue dots) and observed variation (error bars).*

Supplement B. Axial reaction and friction force during sliding

In this section, we scrutinise the numerical evaluation of (19) and (18). It is expedient to change the variable of integration in (19) to r_C via $z = (d_2/2 - r_C)/a_C + Z(t)$ and $\mathrm{d}z = -\mathrm{d}r_C/a_C$, see (14). This gives fixed lower and upper boundaries of integration $r_C = d_1/2$ and $d_2/2$, respectively. The still missing evaluation of $\partial R/\partial z$ is deferred to Supplement C.

Anticipating the constant slope $a_B = -\mathrm{d}r_B/\mathrm{d}z$, the above procedure of transforming the integration variable also applies to (18). Expressing ε likewise, we obtain

$$F_B(t) = 2\pi\,\frac{a_B+\mu}{a_C}\int_{r_1(t)}^{r_2}\big[b_0\,r_C + b(t)\big]\;\sigma_n\Big(1-b_0-\frac{b(t)}{r_C}\Big)\,\mathrm{d}r_C\,, \tag{S 2}$$

$$b_0 = a_B/a_C\,,\quad b(t) = 1/2 - a_B\big[Z(t) + r_2/a_C\big]\,,\quad r_1(t) = r_C\big(-Z(t)\big)\,,\quad r_2 = d_2/2\,. \tag{S 3}$$

The ratio $\mu/a_B \doteq 5.11$ for $\mu = 0.2$ reveals a dominance of the frictional over the compressive contribution to F_B. We can express F_B in closed form upon substitution of (S 1) in (S 2) and integration of the resulting polynomial in r_C. This yields

$$\begin{aligned} F_B(t) = 2\pi\,\frac{a_B+\mu}{a_C}\Big(&\frac{a_0}{2}\big[r_2^2 - r_1^2(t)\big] + a_1\,b(t)\big[r_2 - r_1(t)\big] + a_2\,b^2(t)\ln\Big[\frac{r_2}{r_1(t)}\Big] \\ &- a_3\,b^3(t)\,\big[r_2^{-1} - r_1^{-1}(t)\big] + a_4\,b^4(t)\,\big[r_2^{-2} - r_1^{-2}(t)\big]\Big)\,, \end{aligned} \tag{S 4}$$

with the coefficients $a_{0,1,2,3,4}$ given by

$$\left.\begin{aligned} a_0 &= b_0\big[A(1-b_0)^3 - B(1-b_0)^2 + C(1-b_0)\big]\,,\\ a_1 &= A(1-b_0)^2(1-4b_0) - B(1-b_0)(1-3b_0) + C(1-2b_0)\,,\\ a_2 &= -3A(1-b_0)(1-2b_0) + B(2-3b_0) - C\,,\\ a_3 &= A(3-4b_0) - B\,,\qquad a_4 = A/2\,. \end{aligned}\right\} \tag{S 5}$$

Supplement C. Modelling the stopper's expansion

In the light of its constitutive behaviour, the radial decompression of the stopper occurs in a nonlinear fashion. The two main assumptions underlying its modelling, anticipated in item (v) in § 2.1, are: (I) it

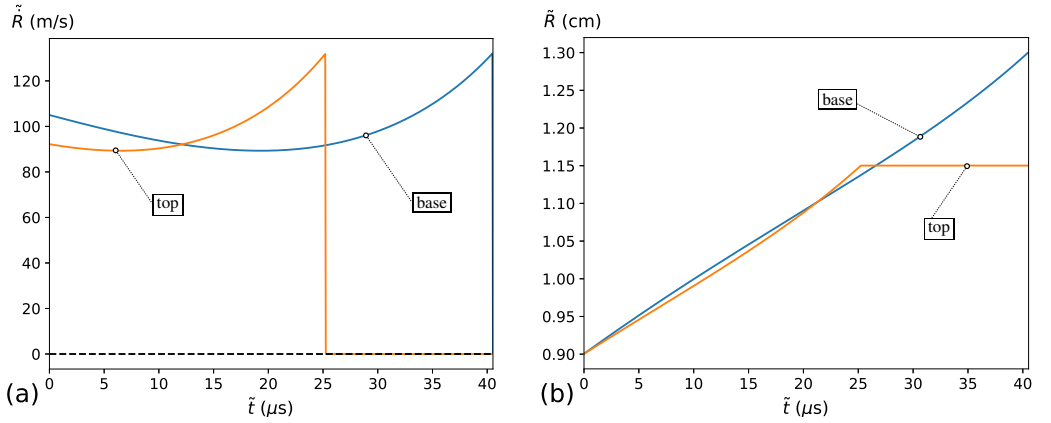

Figure S 2. *Expansion of the stopper: (a) radial speed of base (blue) and top surface (orange); (b) radii of base (blue) and top (orange) vs. $\tilde{t}$.*

starts not earlier as at $t = 0$; (II) it propagates with a speed comparable to that of a hyperelastic (radial-longitudinal) wave, i.e. given by $(\tilde{E}/\tilde{\rho}_C)^{1/2}$ where $\tilde{E} = \mathrm{d}\tilde{\sigma}_n/\mathrm{d}\varepsilon$ is the local bulk modulus of cork and $\tilde{\rho}_C$ its local density, until it has reached its relaxed state. We thus arrive at the modelled dimensionless expansion speed

$$\dot{R}(z,t) = \frac{\partial R}{\partial t} = \sqrt{\frac{1}{\kappa\,\rho_C(z,t)}\,\frac{\mathrm{d}\sigma_n\big(\varepsilon(z,t)\big)}{\mathrm{d}\varepsilon}}\,, \quad \rho_C(z,t) = \rho_C^m\left[\frac{r_C\big(z - Z(t)\big)}{R(z,t)}\right]^2 \tag{S 6}$$

under the constraints $R \le r_C$, $Z(t) \le z \le Z(t) + l_C$, $t \ge 0$. Herein, $\rho_C = \tilde{\rho}_C/\tilde{\rho}_0$ and $\rho_C^m = \tilde{\rho}_C^m/\tilde{\rho}_0$ (see § 2.2). In order to initiate the expansion in a most smooth manner for the sake of numerical stability, the just escaped stopper is conveniently taken as cylindrical:

$$R(z, t \le 0) = \begin{cases} r_B(z) & \big(Z(t) \le z \le 0\big), \\ 1/2 & \big(0 < z \le Z(t) + l_C\big). \end{cases} \tag{S 7}$$

For $t = Z(t) = 0$, we arrive at the initial condition $R(z, t = 0) = 1/2$. This complements (S 6) to a first-order problem governing the temporal variation of R, which is independent of the position of the stopper described by $Z(t)$ and thus decouples from the gas–stopper interaction. Therefore, the radial expansion solely depends on the geometry of the bottleneck apart from the material properties involved.

Given the lossless elastic process it describes, (S 6) raises an oscillatory behaviour. In reality (Liger-Belair et al., 2019), the wavy surface of the stopper associated with its axial movement through the opening is rapidly damped by viscoelastic effects. Despite their entire neglect (last but not least, due to the lack of reliable data), the self-consistency of our simplified model, based on the premises (I) and (II) above, suggests a sufficiently reliable description of the expansion process. In order to suppress unphysically exaggerated oscillations, it is stopped for each value of z at the instance of t where R reaches r_C such that $R = r_C$ for all later times. The relaxation is taken as completed when $R = r_C$ for all values of z along the stopper. We term the time needed to achieve this state relaxation time. Finally, F_b, F_t and F_{ls} in (17) and (19) can be evaluated.

Standard numerical integration of $\dot{R}$ yields a reliable, universal value of approximately $40\,\mu$s for the relaxation time. The expansion of the base and of the top faces of the stopper predicted by our model is visualised in figure S 2.

Supplement D. Technical details of discretisation

Here we provide the interested reader with specific information concerning the numerical discretisation. Emphasis is placed on the dynamics of the stopper.

D.1. Realisation of boundary conditions

At first, we want to support the understanding of the implementation of the boundary conditions, discussed in section 3.2, with the graphical illustration in figure S 3.

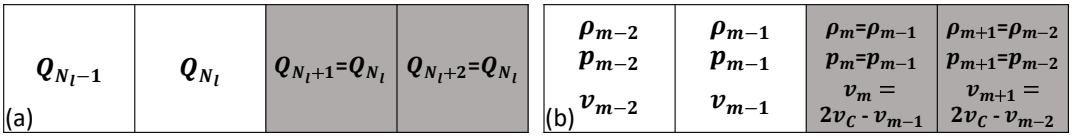

Figure S 3. *(a) Extrapolation condition and (b) no-penetration condition with a boundary velocity of v_C. Ghost cells in both figures are to the right and their total number is $N_G = 2$. N_l is the last cell inside the computational domain and m-1/2 is the surface index of the solid body.*

D.2. Gas–stopper interaction

In order to assign the initial solution vector $\mathbf{Q}^0$ to the correct position on the grid of the computational domain, functions must be defined which return the index of the cell interface nearest to a given point, denoted by the argument of an array inside square brackets. For a two-dimensional array the first index i always refers to the i-th cell interface in the z-direction and the second one j to the index in the r-direction, not depicting their potential dependence on time in any further equation. The opening of the bottle with index b_o and the one for the base surface of the stopper $c_b(t)$ are evaluated by

$$b_o\colon \quad \left|Z_i[b_0]\right| \to \min, \qquad c_b(t)\colon \quad \left|Z_i[c_b(t)] - Z(t)\right| \to \min, \tag{S 8}$$

where Z_i is the array containing all cell interfaces in the z-direction. While b_o and c_b only possess one numerical value for each time step, the indices of the inner surface of the bottle b_{is} and the ones for the lateral surface of the stopper c_{ls} must be defined as an array with index i, including all cell interfaces with an index of j and a position $R_i[j]$ in the r-direction for which the following conditions are fulfilled:

$$\begin{aligned} b_{is}[i]\colon &\quad \left|R_i\left[b_{is}[i]\right] - r_B\left(Z_i[i]\right)\right| \to \min, && i = 0, \ldots, b_o - 1, \\ c_{ls}(t)[i]\colon &\quad \left|R_i\left[c_{ls}(t)[i]\right] - R\left(Z_i[c_b(t) + i], t\right)\right| \to \min, && i = 0, \ldots, c_l - 1. \end{aligned} \tag{S 9}$$

Here $c_l = b_o - c_b(t_0)$ is the total number of cells occupied by the stopper in the z-direction, whereas t_0 is the starting time of the simulation. Here b_o and c_l are excluded because the last interface index corresponds to the first cell centre index outside the given object.

In order to fulfil the given boundary conditions, an indicator field, $\mathrm{ind}[i, j]$, is laid over the computational domain where its values refer to the type of material: 0 to fluid; 1 to bottle; 2 to stopper. Only if the corresponding values between two neighbouring cells are different, the boundary conditions are applied. The initial indicator field, ind^0, has the following form:

$$\mathrm{ind}^0[i, j] = \begin{cases} 1\colon & i = 0, \ldots, b_o - 1, & j = b_{is}[i], \ldots, b_{os}[i] - 1, \\ 2\colon & i = c_b(t_0), \ldots, c_t(t_0) - 1, & j = 0, \ldots, c_{ls}(t_0)[i - c_b(t_0)] - 1, \\ 0\colon & \text{else}. \end{cases} \tag{S 10}$$

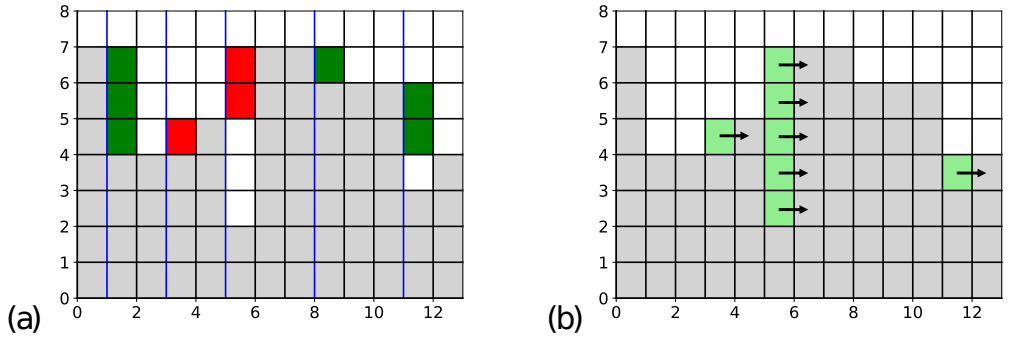

Figure S 4. *(a) Fluid cells contributing to F_{ls}: the stopper occupies the grey cells, the fluid the remaining ones; the red cells reduce and the green ones increase F_{ls}; the blue lines indicate the values of $I_{ls} = \{1, 3, 5, 8, 11\}$. (b) Shifted fluid cells (light-green) due to axial movement of the stopper.*

Here $c_t(t) = c_b(t) + c_l$ is the index of the top interface of the stopper and $b_{os}[i] = b_{is}[i] + \Delta j_b$ are the indices of the outer surface of the bottle with a constant total number of glass cells Δj_b in the r-direction.

The pressure forces on the base and top surface can now be discretised as

$$F_b(t) \approx 2\pi\,\Delta r \sum_{j=0}^{c_{ls}(t)[0]-1} R_i[j]\; p(t)[c_b(t)-1, j]\,, \quad F_t(t) \approx 2\pi\,\Delta r \sum_{j=0}^{c_{ls}(t)[-1]-1} R_i[j]\; p(t)[c_t(t), j]\,, \tag{S 11}$$

where $i = -1$ indicates the last entry, for instance $c_{ls}(t)[\text{–}1] = c_{ls}(t)[c_l - 1]$. Due to the expansion of the stopper being faster than its axial motion, for a short period of time $c_{ls}(t > 0)[0]$ can be bigger than $b_{os}[\text{–}1]$, while $c_b(t > 0)$ is still equal to b_o. Therefore the gas still trapped inside the bottle and the ambient air can both contribute to F_b, splitting the sum in (S 11.1) into

$$\sum_j \to \sum_{j_1} + \sum_{j_2} : \quad j_1 = 0, \ldots, b_{is}[\text{–}1] - 1\,, \quad j_2 = b_{os}[\text{–}1], \ldots, c_{ls}(t)[0] - 1\,. \tag{S 12}$$

While F_b and F_t are integrated over r, the pressure force F_{ls} acting on the lateral surface of the stopper must be integrated over z. This is referenced by the first sum in

$$F_{ls}(t \geq 0) \approx\; 2\pi\,\Delta r \sum_{i \in\, I_{ls}(t)} \sum_j^{\pm} R_i[j]\; p(t)[c_b(t) + i, j]\,. \tag{S 13}$$

The array I_{ls} contains the indices relative to $c_b(t)$ of all fluid cells in the z-direction contributing to F_{ls}. For bigger surface gradients, multiple cells can possess the same entry in I_{ls} (see figure S 4a), explaining the second sum in (S 13), which is defined as

$$\sum_j^{\pm} = \begin{cases} \sum_{j=c_{ls}(t)[i+1]}^{c_{ls}(t)[i-1]-1}: & c_{ls}(t)[i-1] > c_{ls}(t)[i+1]\,, \\ -\sum_{j=c_{ls}(t)[i-1]}^{c_{ls}(t)[i+1]-1}: & c_{ls}(t)[i-1] < c_{ls}(t)[i+1]\,, \end{cases} \qquad i \in I_{ls}(t): \quad 0 < i < c_l - 1\,. \tag{S 14}$$

This distinction is necessary to describe fluid cells acting on left (S 14, top row) and right (S 14, bottom row) interfaces describing the discrete lateral surface of the stopper. As an immediate consequence of its expansion, I_{ls} and therefore also $\sum_j{}^{\pm}$ can change at every time step.

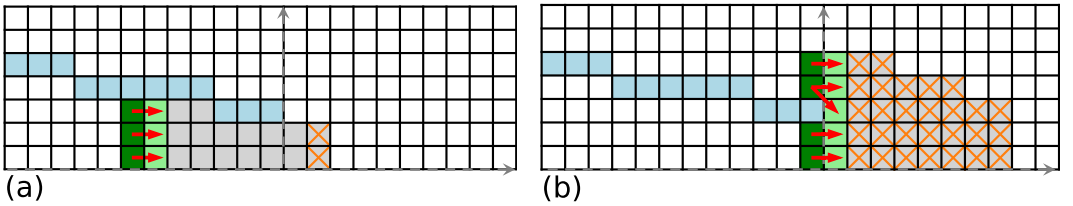

Figure S 5. *Cell updates for $t_n < 0$ (a) and $t_n \geq 0$ (b). The green fluid cells update the light green ones behind the stopper (grey). While the cells of the bottle (blue) keep their initial values, the cells of the stopper marked with orange crosses have to be changed accordingly (ind=2, Q=NaN).*

D.3. Axial motion of the stopper

The spatially continuous motion of the stopper for discrete but variable time steps was already shown in (20). $t_n = 0$ is thereby defined as the point in time, when $c_b(t_n) = b_o$ for the first time. The result in (20) is then used to calculate $c_b(t_{n+1})$ with (S 8), performing the following updates only if $c_b(t_{n+1}) \neq c_b(t_n)$.

1. Check if $c_b(t_{n+1}) - c_b(t_n) = 1$, otherwise the stopper has moved too fast and a smaller Δt_n must be chosen.
2. All values of I_{ls} increase by one due to the stopper moving exactly one cell.
3. The cells behind the stopper are now fluid cells,

$$\mathrm{ind}[c_b(t_n), j] = 0: \qquad j = \begin{cases} 0, \ldots, b_{is}[c_b(t_n)] - 1: & t_n < 0\,, \\ 0, \ldots, c_{ls}(t_n)[0] - 1: & t_n \geq 0\,, \end{cases} \tag{S 15}$$

   and are filled with the same values as the ones to their left:

$$\mathbf{Q}[c_b(t_n), j] = \mathbf{Q}[c_b(t_n) - 1, j]\,. \tag{S 16}$$

4. At that moment when there is only a single cell between the bottle opening and the stopper ($c_b(t_{n+1}) = b_o + 1$) in the z-direction, the values of the cells in between these two objects are taken from the ones above the bottle:

$$\mathbf{Q}\big[b_o, j\big] = \mathbf{Q}\big[b_o - 1, j + \Delta j_b\big]: \qquad j = b_{is}[\text{–}1], \ldots, b_{os}[\text{–}1] - 1\,. \tag{S 17}$$

5. Finally, the cells occupied by the stopper are updated in such a way (see figure S 5) that

$$\left.\begin{aligned} \mathbf{Q}[c_b(t_{n+1}) + i, j] &= \mathrm{NaN}\,, \\ \mathrm{ind}[c_b(t_{n+1}) + i, j] &= 2\,, \end{aligned}\right\}: \quad i,\, j = \begin{cases} c_l - 1, & 0, \ldots, b_{is}[-1] - 1: & t_n < 0\,, \\ 0, \ldots, c_l - 1, & 0, \ldots, c_{ls}(t_{n+1})[i] - 1: & t_n \geq 0\,. \end{cases} \tag{S 18}$$

D.4. Radial expansion of the stopper

While the axial motion of the stopper is characterised by updating c_b, the indices of the lateral surface have to be computed prior to that because when assigning the new ind- and **Q**-values, (S 18) already uses c_{ls} for the new time frame t_{n+1}. The temporally discrete radius of the stopper $R^n[i]$ is spatially continuous with respect to r, but is defined as an array with index $i = 0, \ldots, c_l - 1$, describing its discrete nature with respect to z. The expansion speed $\dot{R}^n$ is evaluated as mentioned in (S 6), exchanging $R(z,t) \to R^n[i]$, $Z(t) \to Z^n$ and $z \to Z_i[c_b(t_n) + i]$. The latter two are the discrete arguments of r_C ($Z_i - Z^n$). $R^{n+1}[i]$ is computed with the explicit Euler method. In a following step, $R^{n+1}[i]$ is used in (S 9.2), finding the solution for $c_{ls}(t_{n+1})[i]$. If $c_{ls}(t_{n+1}) \neq c_{ls}(t_n)$ is true for at least one entry, $I_{ls}(t_{n+1})$ and $\sum_j^{\pm}$ are updated accordingly.

Next, the algorithm for the axial motion of the stopper starts off, updating $\mathbf{Q}$, Z and R, the first two only if necessary. The only exception is the last step, described in (S 18), which must be applied even if the sole discrete motion of the stopper is its radial expansion for the given time frame, increasing the number of cells occupied by the stopper. If the object also or exclusively moves axially at that instant, the whole body is shifted along the z-axis, which requires proper allocation of the new fluid cells (see figure S 4b):

$$\left.\begin{aligned} \mathrm{ind}[c_b(t_{n+1}) + i, j] &= 0\,, \\ \mathbf{Q}[c_b(t_{n+1}) + i, j] &= \mathbf{Q}[c_b(t_n) + i, j] \end{aligned}\right\} : \quad \begin{cases} 0 \le i < c_l - 1, & c_{ls}(t_n)[i] < c_{ls}(t_n)[i+1]\,, \\ & j = c_{ls}(t_n)[i], \ldots, c_{ls}(t_n)[i+1] - 1\,. \end{cases} \tag{S 19}$$

(S 19) is only invoked during the expansion phase since fluid cells need no longer to be shifted along the lateral surface of the stopper after it has reached its relaxed state. Furthermore, it is important that the shift of indices happens before (S 18); otherwise, newly created solid cells are shifted instead.